Statistical model based iterative reconstruction (MBIR) in clinical CT systems. Part II. Experimental assessment of spatial resolution performance

Ke Li
Department of Medical Physics, University of Wisconsin-Madison, 1111 Highland Avenue, Madison, Wisconsin 53705 and Department of Radiology, University of Wisconsin-Madison, 600 Highland Avenue, Madison, Wisconsin 53792

John Garrett and Yongshuai Ge
Department of Medical Physics, University of Wisconsin-Madison, 1111 Highland Avenue, Madison, Wisconsin 53705

Guang-Hong Chen[a)]
Department of Medical Physics, University of Wisconsin-Madison, 1111 Highland Avenue, Madison, Wisconsin 53705 and Department of Radiology, University of Wisconsin-Madison, 600 Highland Avenue, Madison, Wisconsin 53792

(Received 8 March 2014; revised 9 May 2014; accepted for publication 2 June 2014; published 23 June 2014)

Purpose: Statistical model based iterative reconstruction (MBIR) methods have been introduced to clinical CT systems and are being used in some clinical diagnostic applications. The purpose of this paper is to experimentally assess the unique spatial resolution characteristics of this nonlinear reconstruction method and identify its potential impact on the detectabilities and the associated radiation dose levels for specific imaging tasks.

Methods: The thoracic section of a pediatric phantom was repeatedly scanned 50 or 100 times using a 64-slice clinical CT scanner at four different dose levels [$CTDI_{vol}$ =4, 8, 12, 16 (mGy)]. Both filtered backprojection (FBP) and MBIR (Veo®, GE Healthcare, Waukesha, WI) were used for image reconstruction and results were compared with one another. Eight test objects in the phantom with contrast levels ranging from 13 to 1710 HU were used to assess spatial resolution. The axial spatial resolution was quantified with the point spread function (PSF), while the z resolution was quantified with the slice sensitivity profile. Both were measured locally on the test objects and in the image domain. The dependence of spatial resolution on contrast and dose levels was studied. The study also features a systematic investigation of the potential trade-off between spatial resolution and locally defined noise and their joint impact on the overall image quality, which was quantified by the image domain-based channelized Hotelling observer (CHO) detectability index d'.

Results: (1) The axial spatial resolution of MBIR depends on both radiation dose level and image contrast level, whereas it is supposedly independent of these two factors in FBP. The axial spatial resolution of MBIR always improved with an increasing radiation dose level and/or contrast level. (2) The axial spatial resolution of MBIR became equivalent to that of FBP at some transitional contrast level, above which MBIR demonstrated superior spatial resolution than FBP (and vice versa); the value of this transitional contrast highly depended on the dose level. (3) The PSFs of MBIR could be approximated as Gaussian functions with reasonably good accuracy. (4) The z resolution of MBIR showed similar contrast and dose dependence. (5) Noise standard deviation assessed on the edges of objects demonstrated a trade-off with spatial resolution in MBIR. (5) When both spatial resolution and image noise were considered using the CHO analysis, MBIR led to significant improvement in the overall CT image quality for both high and low contrast detection tasks at both standard and low dose levels.

Conclusions: Due to the intrinsic nonlinearity of the MBIR method, many well-known CT spatial resolution and noise properties have been modified. In particular, dose dependence and contrast dependence have been introduced to the spatial resolution of CT images by MBIR. The method has also introduced some novel noise-resolution trade-off not seen in traditional CT images. While the benefits of MBIR regarding the overall image quality, as demonstrated in this work, are significant, the optimal use of this method in clinical practice demands a thorough understanding of its unique physical characteristics. [http://dx.doi.org/10.1118/1.4884038]

Key words: CT, iterative reconstruction, spatial resolution, image quality, model observer

1. INTRODUCTION

The model-based iterative reconstruction (MBIR) framework[1–9] has been introduced to clinical CT systems to reduce patient exposure to ionizing radiation and potentially improve the diagnostic performance of CT scans.[10–13] To maximize the potential clinical benefits of MBIR at the lowest possible radiation dose, CT protocols will have to be specifically optimized for MBIR. Due to the intrinsic nonlinearity of MBIR methods, current CT protocols that may have been optimized for filtered backprojection (FBP) are not directly applicable to MBIR.[14–17] However, the basic principle of CT protocol optimization remains the same for both FBP and MBIR: First, the physical characteristics (e.g., noise variance, noise power spectrum, spatial resolution) of the CT systems need to be quantified using physical phantoms; Second, the dependence of image quality metrics on scanning parameters (e.g., kV, mAs, slice thickness) needs to be understood both experimentally and theoretically if possible; Third, clinical diagnostic imaging tasks need to be identified and the relationship between image quality metrics measured by physicists and diagnostic quality as assessed by radiologists should be established. This enables translation from image quality requirement for each specific task to scanning parameters; Fourth, CT scanning parameters are prescribed to generate images with desirable qualities that meet the requirement of clinicians; Fifth, the prescribed protocols need to be continuously reviewed and refined by a joint group of clinicians, medical physicists, and technologists to ensure they are repeatable, robust, implementable, and relevant.

MBIR has posed some new challenges to the second and the third steps in the aforementioned framework due to its nonlinearity and related unique image quality characteristics.[14–17] For example, several studies have reported significant reduction in noise magnitude when compared to FBP.[14,16,17] It has been found that with MBIR the magnitude of noise reduction is related to the radiation dose level through a power law.[17] Further, these studies found that the amount of spatial noise correlation increases in MBIR images, which was demonstrated in the spatial frequency domain as a shift of the peak of the noise power spectrum (NPS) toward lower spatial frequencies with the amount of shift related to the radiation dose through a power law.[17]

The nonlinear nature of MBIR methods has introduced significant challenges to the characterization of spatial resolution performance. For example, conventional modulation transfer function (MTF) measurements based on small high contrast objects (typically a metal wire) are no longer applicable to objects with low and intermediate contrast levels.[15] Richard *et al.* have developed a task-based framework to quantify the spatial resolution of MBIR.[15] In this framework, a concept of task-specific MTF, MTF_{Task}, was introduced to locally measure the MTF for a given feature of interest (FOI) at a given radiation dose level. When the contrast of the FOI or the radiation dose level are relatively low, the reduced contrast-to-noise ratio (CNR) may prevent one from obtaining an accurate and reliable extraction of the spatial resolution information from the noisy background. Similar results were reported in other work discussing other iterative reconstruction (IR) algorithms.[18]

In this paper, we developed a different measurement method to systematically study the spatial resolution performance of MBIR. The method reduces the statistical uncertainty of measurement by performing an ensemble averaging of repeated CT scans, which allows the spatial resolution performance at the edges of non-cylindrical and/or low contrast objects to be reliably quantified even at low dose level. The method operates locally near the FOI in the image domain, thus it does not require the spatial resolution of the CT system to be shift-invariant.

Using this method, we experimentally characterized the spatial resolution performance of a commercially available implementation of MBIR (Veo®, GE Healthcare, Waukesha, WI) that has been equipped on several state-of-the-art clinical CT scanners at our institution. The characterization covered four exposure levels and eight contrast levels as low as 13 HU. Since earlier studies have shown that phantoms with relatively simple structures may not be representative of the physical performance of IR methods,[19] our study used an anthropomorphic pediatric phantom containing inhomogeneous and irregular interfaces between anatomical structures. Further, it is worth emphasizing that the ultimate goal of characterizing noise and spatial resolution is to understand how they jointly impact performance for a diagnostic imaging task. Therefore, systematic investigations were also performed to study the tradeoff between spatial resolution and noise in MBIR and their joint contributions to the overall image quality, which was quantified by the image-domain channelized Hotelling observer (CHO) detectability index. Finally, another novel contribution of this work is an experimental assessment of the z resolution (i.e., slice sensitivity) of MBIR at both low and high contrast levels. All of the characterizations of MBIR were accompanied by the characterizations of FBP under identical experimental conditions for comparison.

2. METHODS AND MATERIALS

2.A. Experimental phantom data acquisition

In this study, we used a 64-slice clinical diagnostic CT scanner (Discovery CT750 HD, GE Healthcare, Waukesha, WI) equipped with both the FBP and the Veo reconstruction engine to repeatedly scan the chest section of a pediatric phantom (Section 16, ATOM 10-year-old pediatric phantom, Model 706, CIRS Inc., Norfolk, VA). The physical dimensions of cross-section of the phantom at this position are approximately 20 cm (AP) × 17 cm (LR). To avoid misregistration caused by table motion between repeated scans, the phantom was scanned in the axial scanning mode and the scan range was set to be equal to the detector coverage (20 mm). For the version of Veo installed at our institution, only a Head (including pediatric and small head) scanning field of view (SFOV) is compatible with the axial scanning mode, and thus was chosen in this study. The gantry rotation time was set to 0.5 s and the tube potential was set to

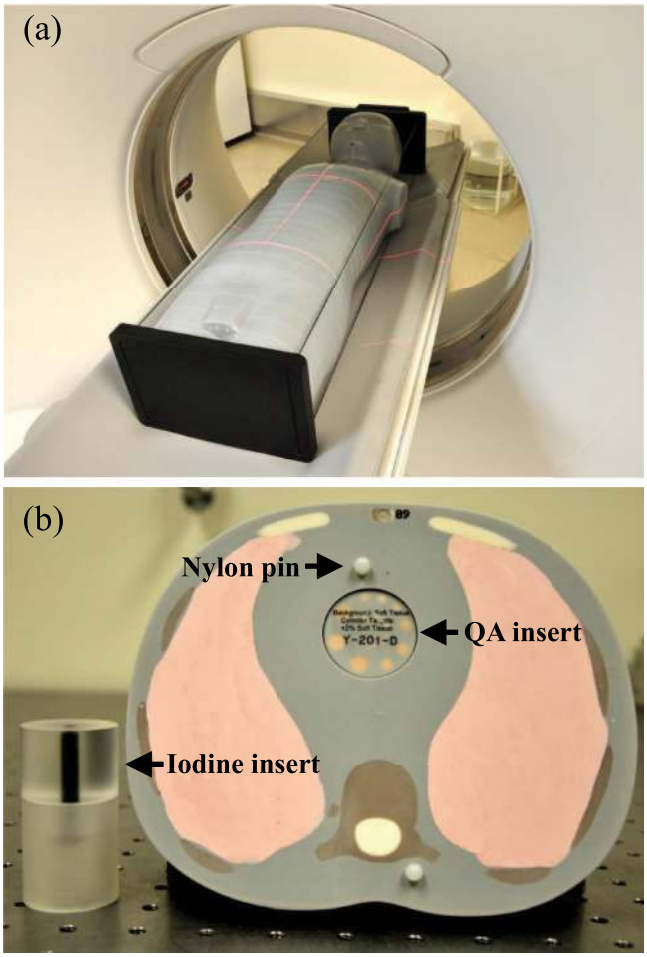

FIG. 1. (a) The anthropomorphic phantom used in our study. (b) A section (#16) of the phantom and two plug inserts. Iodine solution filled in one of the plugs was dyed with a black ink for illustrative purposes.

120 kV. The scans were performed at four different mA levels (40, 80, 120, 160), which correspond to $CTDI_{vol}$ levels of 3.99, 7.99, 11.98, 15.97 mGy, respectively (measured with the 16 cm CTDI phantom). These exposure levels will be referred to throughout this paper as 25%, 50%, 75%, and 100% dose, respectively. The acquired data were reconstructed using both FBP and Veo. The reconstruction slice thickness was 0.625 mm. For FBP, the standard reconstruction kernel was used and the image matrix size is 512 × 512. For the current version of Veo, the reconstruction matrix size is 1024 × 1024 if the axial scanning mode is used.

The spatial resolution was evaluated locally at several representative feature of interests (FOIs) in the phantom, including a Nylon pin and the anatomical interfaces of lung tissue/bone and lung tissue/soft tissue (Fig. 1). In addition, a Ø = 37 mm factory QA insert that contains cylindrical targets with two different contrasts values (13 and 33 HU) was used (Soft tissue insert-cylindrical targets, Model 700-QA, CIRS Inc., Norfolk, VA). Similarly, a Ø = 38 mm inhouse acrylic phantom insert that contains Ø = 5.0 mm cylindrical cavity was used. The cavity was filled with different dilutions of Visipaque™–320 (GE Healthcare, Waukesha, WI) and deionized water providing three different concentrations of iodine (0, 11.2, and 16 mg I/ml) to provide three additional contrasts. The bottom of the cavity was machined flat to generate a sharp step function along the z direction. This design allowed us to quantify the z resolution for specific contrast levels. Overall, the study covered FOIs with a total of eight contrast levels to study the contrast dependence of the spatial resolution of Veo. The experimentally measured contrast values of these FOIs are listed in Table I.

TABLE I. List of measured CT contrast values of eight FOIs in the phantom.

	Material	Background	Contrast (HU)
Object 1	+1% Soft tissue	Soft tissue	13
Object 2	+2% Soft tissue	Soft tissue	33
Object 3	Nylon	Soft tissue	62
Object 4	Water	PMMA	120
Object 5	11 mg/ml I	PMMA	224
Object 6	16 mg/ml I	PMMA	346
Object 7	Soft tissue	Lung	814
Object 8	Bone	Lung	1710

When the factory QA inserts were used, the phantom was repeated scanned 100 times at each dose level; when the inhouse iodine insert was used instead, the number of repetitions was reduced to 50 due to its relatively high CNR. The image ensembles produced by repeated scans were used for spatial resolution, noise, and model observer analysis.

2.B. Axial spatial resolution measurement method

The classical definition of spatial resolution is the capacity of an imaging system to distinguish two objects as they become smaller and closer together.[20] The spatial resolution of an image can be quantified either by the point spread function (PSF) in the spatial domain or by the MTF in the frequency domain. The MTF is often considered a more convenient descriptor of spatial resolution, because it can be represented as the products of MTFs of subimaging stages[15,20–22] and is easily translated to the practical concept of resolvable line-pairs/cm (lp/cm) since the $MTF_{10\%} \approx$ resolvable lp/cm. For nonlinear IR methods, such as Veo, however, the use of the MTF as the description of spatial resolution has been challenged, as there is no guarantee of shift-invariance in images generated with these methods. In this case, the frequency domain analysis method loses its advantage over the spatial domain analysis method. As a result, we chose to characterize the spatial resolution of Veo reconstruction in the spatial domain using PSF. In addition, we chose to define the PSF locally in the CT image due to possible shift variance introduced by the IR method. The PSF was measured for each FOI at each dose level using the following definition:

$$\mathrm{PSF}(x_\perp) = \frac{\mathrm{d}I(x_\perp)/\mathrm{d}x_\perp}{\int \mathrm{d}x_\perp \{\mathrm{d}I(x_\perp)/\mathrm{d}x_\perp\}}, \quad (1)$$

where $x_\perp$ denotes the direction orthogonal to the edge of interest, I denotes image pixel value with a unit of [HU]. Traditionally, the PSF has often been measured using circular objects so that any line going through the object center runs normal to

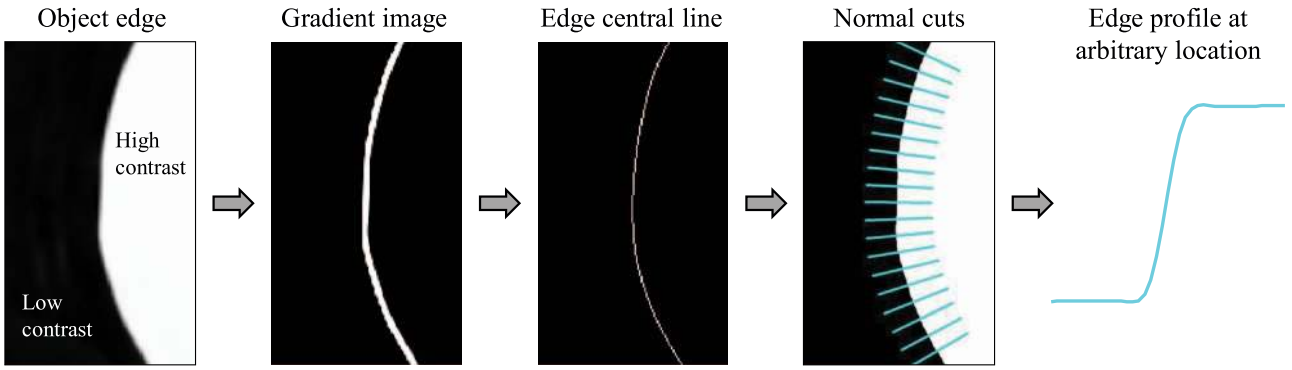

FIG. 2. The work flow of spatial resolution measurements using irregularly shaped test objects.

the edge. In comparison, the extraction of $I(x_\perp)$ from irregularly shaped objects is relatively more challenging. This work developed the following method to measure the edge profile of an arbitrarily shaped object (Fig. 2):

(i) Perform ensemble averaging for a single axial plane;
(ii) Take spatial derivative of the averaged low noise image along both the x and y directions and form a gradient image by calculating the amplitude of the gradient;
(iii) Identify the edge central line $y_c(x)$ by tracking the maximum value in the gradient image;
(iv) Perform denoising/smoothing of the edge central line. In this paper, a fifth degree polynomial was used to fit the curve;
(v) Differentiate $y_c(x)$ with respect to x to get the tangent direction at each point on the central line;
(vi) Calculate the angle θ of the normal line at each point using $\tan[\theta(x)] = -1/y_c'(x)$;
(vii) Based on the angle θ and the edge central line $[x, y_c(x)]$, extract line profiles running normal to the edge. In our implementation, the line profiles were ± 2.2 mm across the center of the edge;
(viii) Average the edge profile from multiple points on the edge to further reduce noise. The last step is optional and can be used in the case of ultra-low CNR to improve accuracy.

While the entire PSF curve is valuable in characterizing spatial resolution, there is often a need to extract a single numerical figure of merit (FOM) to quantify the spatial resolution. For example, the spatial frequencies corresponding to the 50% and 10% MTF values (i.e., f_{50} and f_{10}, respectively) are often used as the FOMs of spatial resolution.[15] To enable the use of a spatial domain FOM of spatial resolution, the PSFs of Veo reconstructions were modeled as Gaussian functions, the width of which was quantified with a parameter, w,

$$\mathrm{PSF}'_w(x_\perp) = \frac{1}{\sqrt{2\pi}\,w}\exp\left(-\frac{x_\perp^2}{2w^2}\right). \tag{2}$$

In this work, w was used as the FOM of spatial resolution. It was determined from experimental PSF by solving the following least squares problem:

$$\hat{w} = \arg\min_w \left\|\mathrm{PSF}'_w(x_\perp) - \mathrm{PSF}(x_\perp)\right\|_2^2, \tag{3}$$

where $\|\cdot\|_2$ denotes the Euclidean norm. A smaller w value represents a superior spatial resolution (e.g., sharper edge). For the case of FBP (with standard reconstruction kernel), the Gaussian model has been validated to be a good approximation of the PSF.[23,24] We revisited the feasibility and accuracy of this model in Veo reconstructions by calculating the relative root mean square error (rRMSE),

$$\mathrm{rRMSE} = \frac{\left\|\mathrm{PSF}'_w - \mathrm{PSF}\right\|}{\sqrt{N}[\max(\mathrm{PSF}) - \min(\mathrm{PSF})]} \times 100\%, \tag{4}$$

in which N is the total number of elements in a digitized PSF curve.

2.C. Slice thickness (z resolution) measurement method

The z resolution of CT systems can be quantified with the slice sensitivity profile (SSP), which is often generated by scanning high contrast metal beads, thin discs, or ramps. In this work, we were interested in measuring the SSP of Veo at relatively low contrast levels. To achieve this goal, the bottom of the cavity in the inhouse acrylic phantom insert was machined to be flat. This design allows the acrylic and the liquid filled in the cavity to form a sharp step function along the z direction. In our study, the cavity was filled with water or iodine solution (13 mg/ml) to generate two contrast levels (120 and 270 HU) inside the anthropomorphic phantom. Under the guidance of the localizer radiographs (scout images), the phantom was carefully positioned so that the edge was perpendicular to the z axis of the CT system. At each contrast level, repeated scans were performed using the aforementioned scanning protocols (50 repetitions $\times$ 4 dose levels). Ensemble averaging was performed for each contrast and dose level to reduce noise.

To increase the number of discrete sampling point along the z direction, the 0.625 mm CT slices generated by the axial scans was retrospectively resampled to a 0.1 mm slice interval using linear interpolation. This is different from the helical scan case, which enables finer slice sampling by performing multiple reconstructions at arbitrary slice locations. The resampled axial slices were reformatted to coronal slices before the slice that cuts through the central axis of the cavity was

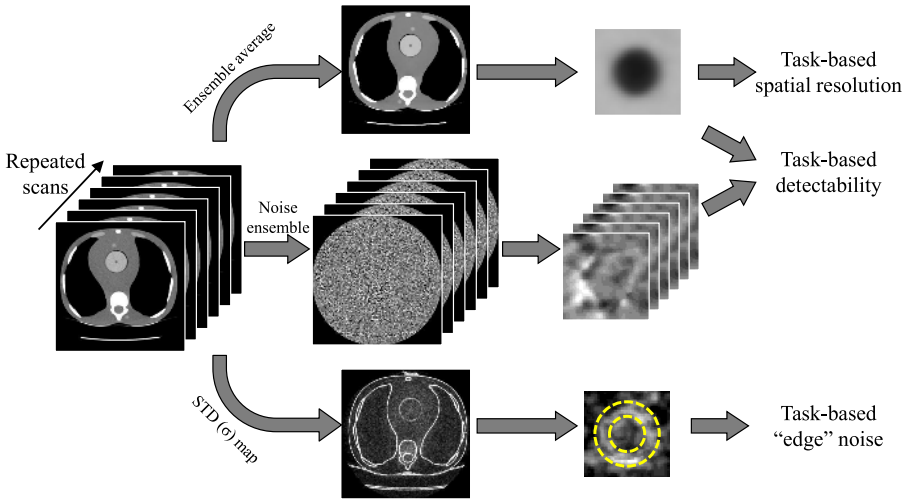

FIG. 3. Work flow for task-based and local assessments of spatial resolution, noise, and model observer detectability from an ensemble of images. The so-called "edge noise" was defined in the region bounded by the dashed circles.

identified. The line profile that ran across the edge, $I(z)$, was used to generate the SSP,

$$\mathrm{SSP}(z) = \frac{\mathrm{d}I(z)/\mathrm{d}z}{\int \mathrm{d}z\,\{\mathrm{d}I(z)/\mathrm{d}z\}}. \tag{5}$$

The full width at half maximum (FWHM) of the SSP was used as the FOM to characterize slice thickness. The FWHM of the SSP of FBP images was compared with the value provided by the CT manufacturer (0.69 at 20 mm detector collimation, 0.625 mm reconstruction slice thickness, axial scan mode) to validate the measurement method.

2.D. The tradeoff of spatial resolution with edge noise

Spatial resolution of CT images cannot be measured and meaningfully interpreted without specifying image noise, and vice versa. A "soft" reconstruction kernel in FBP usually generates CT images with lower noise amplitude, but poorer spatial resolution, whereas an "edge-enhancing" reconstruction kernel usually leads to higher noise but sharper edges. The linearity of FBP determines that the reconstruction/data processing parameters will always influence signal and noise in the same way. That said, when the CT system, reconstruction kernel, and scanning parameters (other than exposure level) are fixed, spatial resolution remains approximately constant, while image noise depends strongly on exposure level and image object. In this case, spatial resolution is generally considered to have no tradeoff with image noise, although the accuracy of the spatial resolution measurement does depend on the noise level.

For the highly nonlinear Veo method, however, it is possible that an additional tradeoff relationship between spatial resolution and image noise has been introduced: higher dose may simultaneously enhance spatial resolution[15] and reduce image noise.[14–17] To investigate this potential interplay between noise and spatial resolution, we measured noise standard deviation value σ locally on the edges of FOIs where spatial resolution was assessed with the help of the acquired image ensembles:

$$\sigma(x, y) = \sqrt{\frac{1}{M-1}\sum_{i=1}^{M}[I_i(x, y) - \bar{I}(x, y)]^2}, \tag{6}$$

in which M is the total number of scan repetition, and the mean image pixel value $\bar{I}$ is given by

$$\bar{I}(x, y) = \frac{1}{M}\sum_{i=1}^{M} I_i(x, y). \tag{7}$$

This method enables the quantification of the expected σ value at each point in the image, including those on the edges of the FOIs. σ values in the vicinity (± 2 pixels) of the central line of the edge for each FOI were averaged to estimate the "edge" noise (Fig. 3).

2.E. Channelized Hotelling observer method

Neither spatial resolution nor image noise provides a complete description of image quality. A FOM for the overall image quality that includes the joint contributions of spatial resolution and noise is needed. In this work, we employed the channelized Hotelling observer (CHO) analysis method[25–28] and used the CHO detectability index (a.k.a. CHO signal-to-noise ratio)[25,26,29] as the FOM to characterize the overall image quality. The CHO method has been validated by human observers to work with CT images generated by some specific types of nonlinear iterative reconstruction method for a signal known/location known detection task.[30] In this work, we only use the CHO detectability index as a metric to incorporate both spatial resolution and noise into the analysis. The correlation between the CHO model observer performance and the human observer performance is interesting and important to study, but is beyond the scope of this paper.

The CHO analysis method uses a set of channel basis functions (t_i, $i \in [1, 2, \ldots m]$) to decompose images. As a result, the

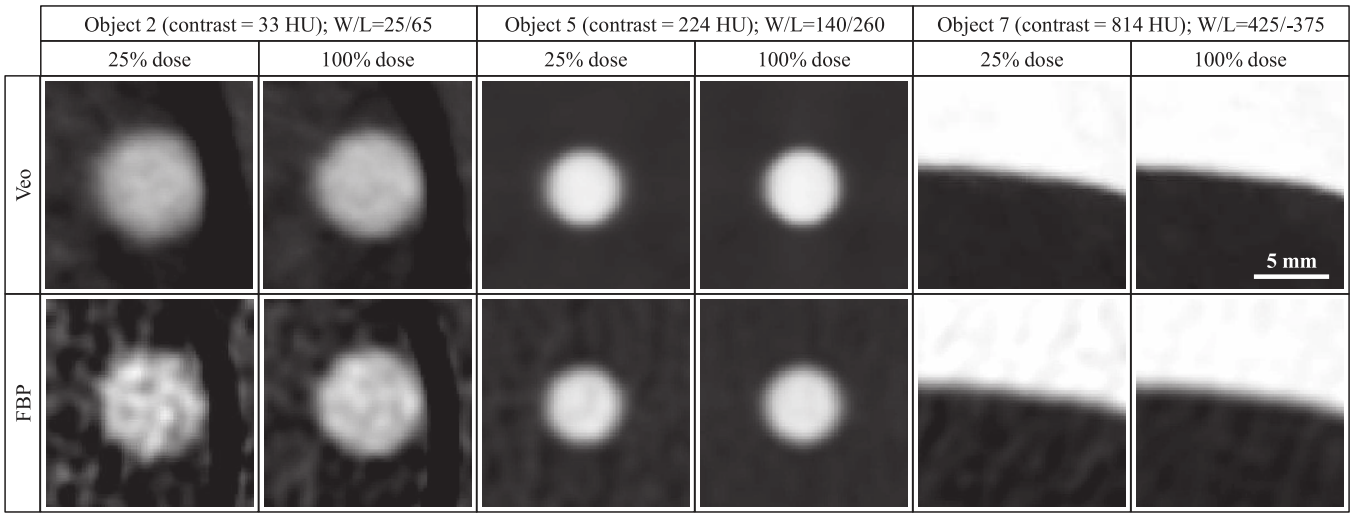

FIG. 4. Representative low-noise region-of-interest (ROI) images used to measure the spatial resolution of Veo and FBP. The images represent an ensemble average of consecutive scans. The scale bar applies to each of the images above.

covariance matrix, **K**, as seen by the channel basis, is given by[25]

$$\mathbf{K_c} = \mathbf{T^t K T}, \tag{8}$$

in which the columns of matrix **T** correspond to each of the vectorized channel function t_i. Similarly, the imaging task vector, **s**, after seen through the channel basis, is given by[25]

$$\mathbf{s_c} = \mathbf{T^t s}. \tag{9}$$

The square of the detectability index (denoted by d') is given by[25,26,29]

$$(d')^2 = \mathbf{s_c^t}\,\mathbf{K_c^{-1}}\,\mathbf{s_c}, \tag{10}$$

The detectability index d' incorporates the noise performance of the image through the covariance matrix **K** and the spatial resolution performance through the signal vector **s**. In this work, the CHO method was implemented using the Gabor channel basis, which has been previous validated to have a close resemblance to human observer responses.[30] Parameters of the channel basis functions (e.g., central frequency, bandwidth, cutoff frequency, etc.) were chosen to be consistent with Ref. 30.

The CHO analyses were performed for the first six FOIs in Table I with low or intermediate contrast. The imaging task, s, was defined statistically from the ensemble of repeated scans as

$$s(x, y) = \bar{I}_{\text{object}}(x, y) - \bar{I}_{\text{bkgd}}(x, y), \tag{11}$$

where the mean signal-present image $\bar{I}_{\text{object}}$ was measured in a 13×13 mm^2 local region containing the object, and the mean signal-absent image $\bar{I}_{\text{bkgd}}$ was measured in a 13×13 mm^2 region immediately adjacent to, but not containing, each object.

As a summary of the experimental method, CT image ensembles generated from repeated data acquisitions were used to perform task-based and locally-bounded measurements of spatial resolution, edge noise, and CHO detectability. All measurements were performed in the image domain. Figure 3 summarizes the work flow for these measurements.

3. RESULTS

3.A. Validation of the Gaussian model

Figure 4 shows the mean images of three features of interest. The noise level in these images was significantly reduced by ensemble averaging to facilitate accurate spatial resolution measurements and to help directly visualize the sharpness of the edges. The PSFs and the Gaussian fitting results measured at 25% dose level are presented in Fig. 5, which clearly demonstrate the contrast-dependence of the PSF curves of Veo reconstructions and also the good accuracy of the Gaussian model. All rRMSE values listed in Table II are below 3%. We did not perform Gaussian fitting to the FBP images of the ultra-low-contrast Object 1 because of the low CNR [Fig. 5(a)]. However, the PSFs of FBP measured at all other contrast levels in Fig. 5 demonstrated that they are independent of contrast level.

3.B. Contrast dependence of spatial resolution

The contrast dependence of the spatial resolution of Veo can be directly visualized from the averaged ROI images in Fig. 4: For Object 2 with relatively low contrast, its edges appears to be more blurred in the Veo images than in the FBP images; For Object 5 with intermediate contrast, the sharpness of its edge is equivalent (e.g., at 25% dose) or slightly better (e.g., at 100% dose) in Veo images than in FBP images; For the interface between tissue and lung (Object 7) with relatively high contrast, Veo led to better edge sharpness than FBP.

The PSF curves shown in Fig. 5 also demonstrate the contrast dependence of spatial resolution of Veo reconstructions. The spatial span (width) of the PSF measured with low contrast Object 1 is significantly wider than that measured with

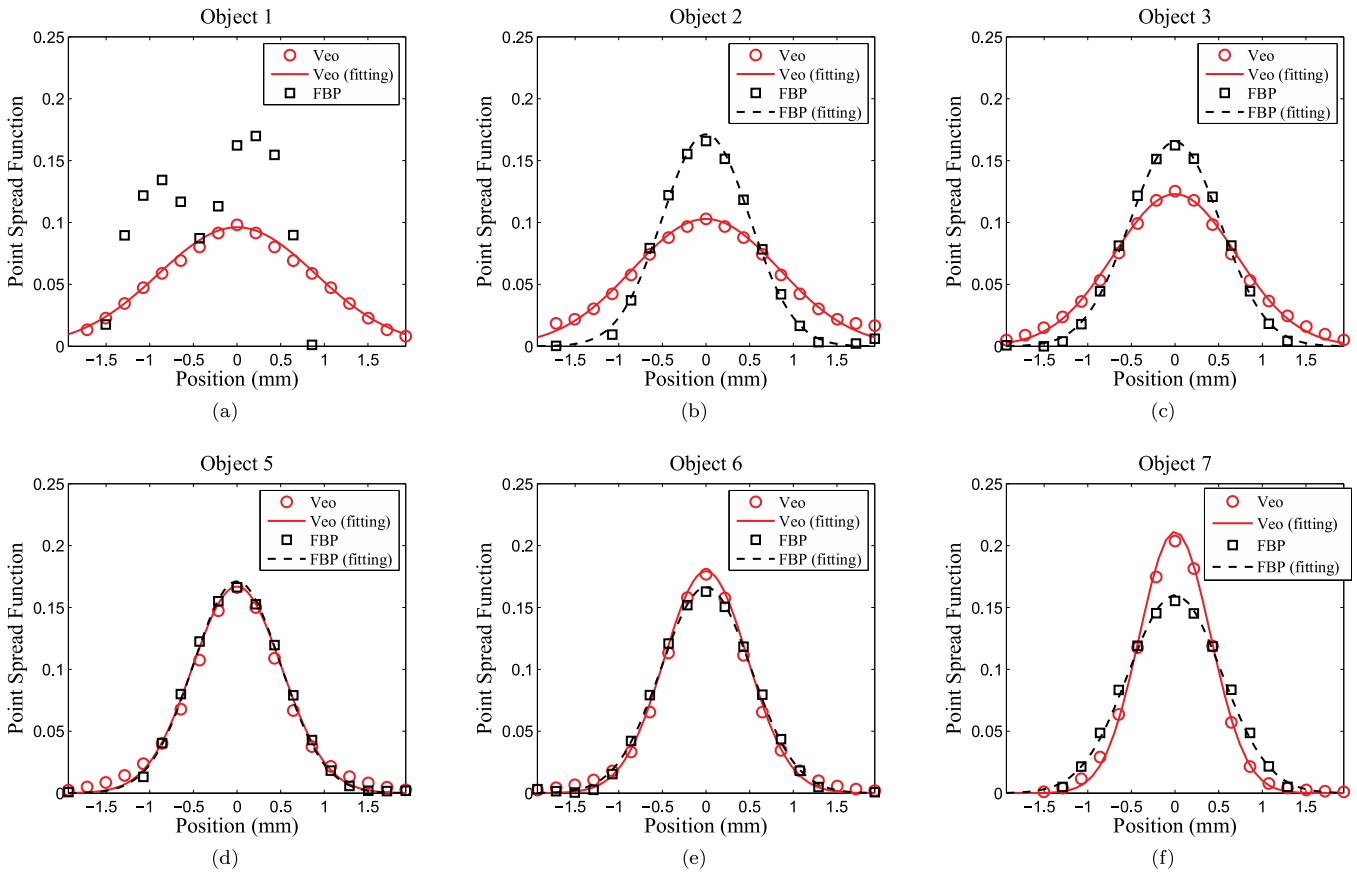

FIG. 5. Representative experimental PSFs measured at 25% dose level and the corresponding Gaussian fitting results for objects of increasing contrast levels. The plot in (a) corresponds to the lowest contrast level, while the plot in (f) corresponds to the highest. The PSF of FBP measured with the ultra-low contrast Object 1 in (a) was too noisy to enable the fitting.

the high contrast Object 7. The PSFs of Veo and FBP became equivalent for Object 5 with a contrast of 224 HU. As shown later in Sec. 3.C, this transitional contrast is highly dose dependent.

3.C. Radiation dose dependence of spatial resolution

The low noise ROI images in Fig. 4 also demonstrate that the spatial resolution of Veo is dose dependent. For example, the Veo image of Object 1 measured at 100% dose looks sharper than that measured at 25% dose. This visual observation was confirmed by the quantitative PSF results presented in Fig. 6. The decrease in the w values of Veo reconstructions, when the dose was increased from 25% to 100%, was 0.11 mm for Object 4 and 0.10 mm for Object 6. In comparison, the spatial resolution of FBP reconstructions is independent of radiation dose level [Fig. 6(c)]. The widths of the PSFs (w) of Veo and FBP became equivalent at certain dose level; w of Veo assessed using low contrast objects required higher dose level to surpass the w of FBP.

Figure 7 summarizes the joint dependence of the spatial resolution of Veo reconstructions on contrast and radiation dose levels. The width of the PSF, w, increases monotonically with decreasing contrast and decreasing dose; the w value at 100% dose and 1280 HU is 0.33 mm, which is only 37% of the w value measured at 25% dose and 13 HU. In comparison, the spatial resolution of FBP is independent of radiation dose and contrast level; the mean w value of FBP is 0.52 mm and the 95% confidence interval (CI) of the mean is [0.49, 0.55] mm. By (linearly) interpolating data measured at the eight contrast levels, the "crossover" contrast at which the spatial resolutions of Veo and FBP became equivalent was calculated. The crossover contrast is strongly dose dependent and is 300 HU at 25% dose, 174 HU at 50% dose, 127 HU at 75% dose, or 78 HU at 100% dose.

TABLE II. Relative root mean square error (rRMSE) of the Gaussian model for the PSF of Veo reconstructions.

		Dose (%)			
Object #	Contrast (HU)	25	50	75	100
1	13	2.2	1.1	1.5	0.9
2	33	1.3	0.9	0.9	0.7
3	62	0.9	0.5	0.6	0.6
4	120	1.1	0.9	0.9	1.0
5	224	0.8	0.6	0.6	0.6
6	346	0.5	0.4	0.4	0.3
7	814	0.4	0.3	0.2	0.3
8	1710	0.7	0.7	0.7	0.7

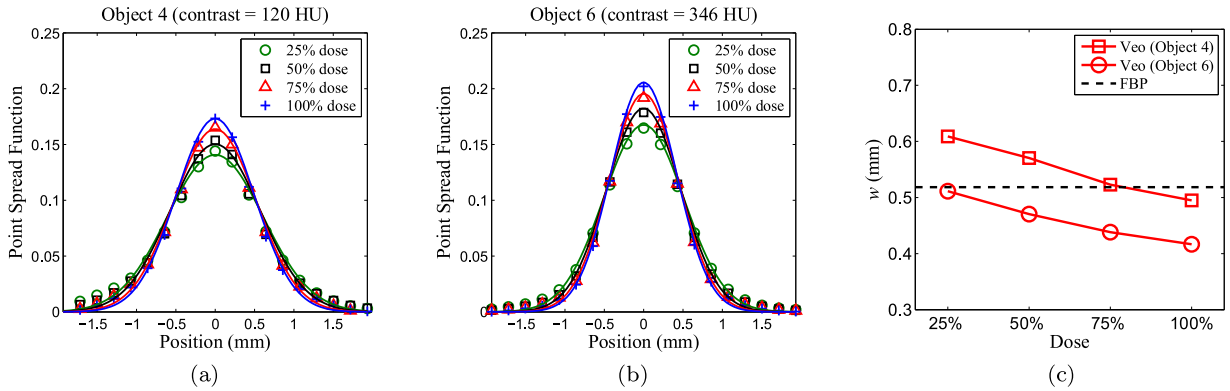

FIG. 6. (a) and (b) Representative PSFs of Veo measured at four different dose levels. The solid lines are Gaussian fits of the experimental data. (c) Plots of the FOM of spatial resolution (w) as a function of dose.

3.D. Spatial resolution along *z*

Figure 8 shows SSP of Veo measured at two contrast levels (120 and 270 HU) and four dose levels. The SSP of FBP measured at the 100% dose level is also presented in the same figure. The FWHMs of the SSPs are listed in Table III. For FBP, the FWHM of the SSP is independent of the contrast or dose levels, and its value (0.69 ± 0.01 mm) is consistent with the number specified in the user manual of the CT system (0.69 mm). This agreement also validates the proposed slice thickness measurement method used in this work. In contrast, for Veo, the SSP demonstrated a dependence on both contrast and dose levels: the SSPs assessed at contrast = 270 HU are consistently sharper than those at 120 HU; this was confirmed by the FWHM values in Table III. The SSP of Veo also exhibited a dependence on dose at the lower contrast level (120 HU): its width increased monotonically with decreasing dose level. At the higher contrast level (270 HU), the dose dependence of the SSP was negligible.

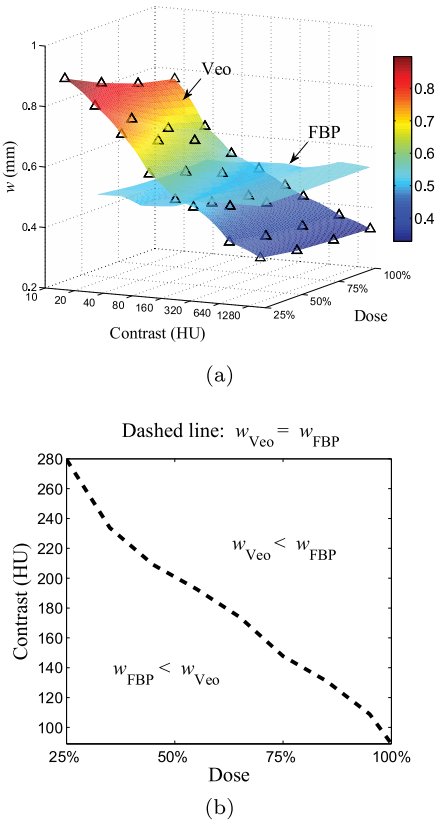

FIG. 7. (a) Summary of the contrast- and dose-dependence of the FOM of spatial resolution (w). The triangles represent the experimental data points, from which other data points were estimated using two-dimensional linear interpolation. (b) Dose dependence of the crossover contrast at which the spatial resolutions of Veo and FBP were found to be equivalent.

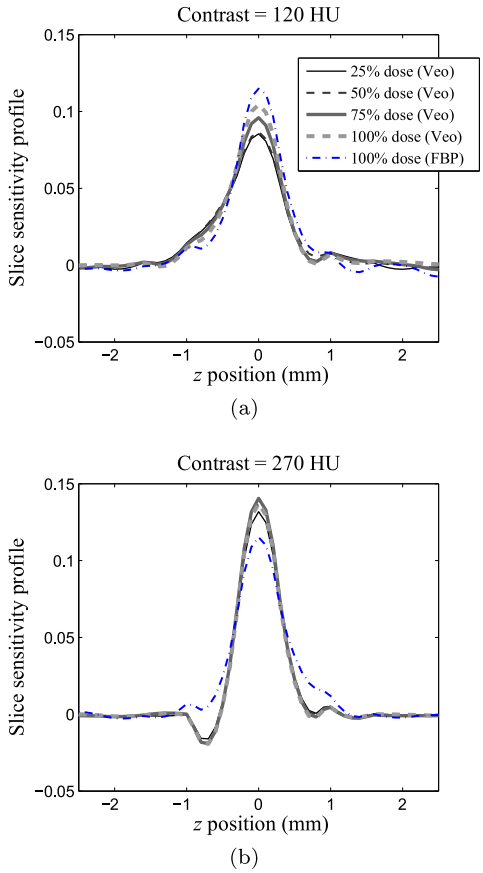

FIG. 8. The SSP assessed at two contrast levels and four dose levels. The legend in (a) also applies to (b).

TABLE III. Slice thickness quantified by the FWHM (in mm) of the SSP. The reconstruction slice thickness is 0.625 mm.

		Dose (%)			
Method	Contrast (HU)	25	50	75	100
Veo	120	0.81	0.81	0.75	0.72
	270	0.61	0.61	0.61	0.61
FBP	120	0.68	0.70	0.68	0.68
	270	0.70	0.70	0.70	0.70

3.E. Spatial resolution-noise tradeoff

Noise standard deviation (σ) maps measured locally in three of the FOIs using Eq. (6) at the 25% dose level are shown in Fig. 9. Note that the display level used for the σ maps of Veo is only 31% of that of FBP, which indicates that images generated by Veo have much smaller noise magnitude than FBP. However, noise in Veo images demonstrated a strong contrast dependence: for noise right on the edge, it increased with an increasing contrast level; for noise in other uniform regions, its value remained independent of contrast level. This suggests that edge noise in Veo has a strong contrast dependence even when the dose level is fixed. Figure 10(a) summarizes this phenomenon by plotting σ as a function of both contrast and dose level. This figure was obtained by performing 2D interpolation from 32 experimental data points (4 dose levels $\times$ 8 contrast levels). It clearly demonstrates that, in addition to the well-known dose dependence, noise of Veo images measured locally at the edges of objects increased with increasing contrast level at any dose level. This is fundamentally different from the case of FBP reconstruction, which usually demonstrates the same noise magnitude for edge regions and uniform regions.

Previous studies have demonstrated that Veo leads to significant noise reduction in uniform regions of test objects.[14,16,17] An immediate question based on the results in Fig. 10(a) is, how does the noise magnitude of Veo reconstructions compared with that of FBP reconstructions if the noise was strictly measured on the edges of test objects?

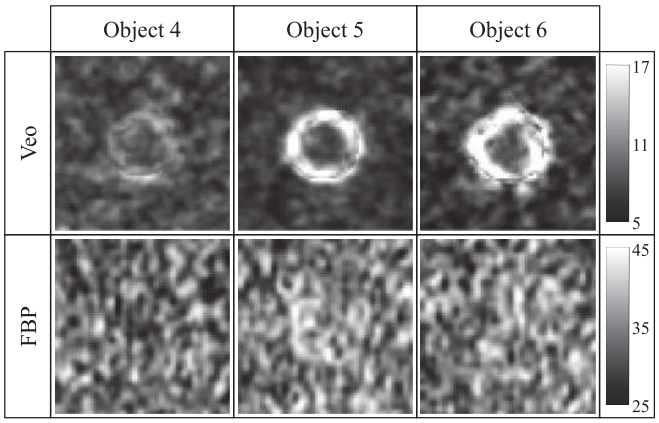

FIG. 9. Noise standard deviation (σ) maps measured at 25% dose in the neighborhood of three representative objects. The noise magnitude on the edges of these objects demonstrated a strong contrast dependence in Veo.

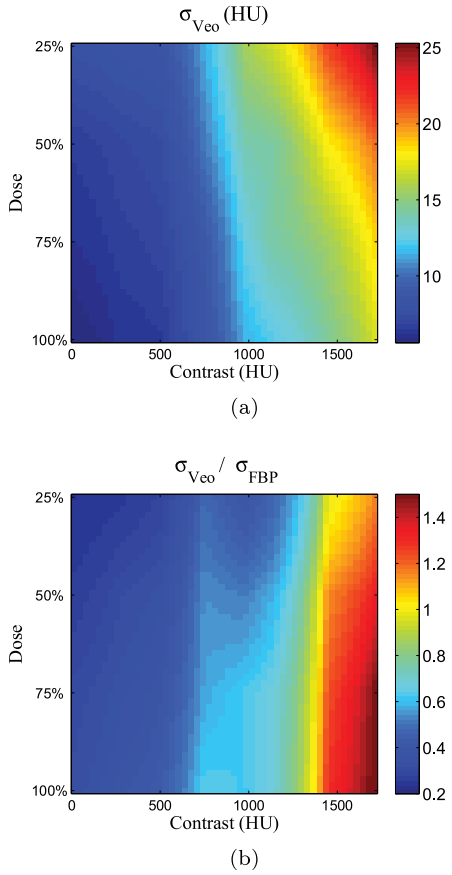

FIG. 10. Summary of the contrast- and dose-dependence of the noise standard deviation (σ) measured locally at the edges of test objects. (a) Absolute σ of Veo; (b) Ratio of σ between Veo and FBP.

To address this question, the noise standard deviation of Veo images (σ_{Veo}) was normalized by that of FBP images (σ_{FBP}) measured at each dose/contrast level and the results are shown in Fig. 10(b). It demonstrates that, even when the noise was assessed right on the edges of test objects, in most cases Veo still led to significant reductions in noise. Only when the contrast level exceeded 1300 HU did Veo generate higher edge noise than FBP. The crossover contrast increased slightly with decreasing dose level.

Results in Figs. 10(b) and 7(a) demonstrate that spatial resolution and noise measured on the same location have certain tradeoff in Veo. Low contrast/low dose conditions always led to more aggressive noise reduction, but they also tended to generate relatively inferior spatial resolution. Similarly, high contrast/high dose conditions always led to a smaller reduction in noise (sometimes even resulting in a minor noise amplification) in order to achieve superior spatial resolution.

3.F. CHO detectability

The observed interplay between spatial resolution and noise performances in Veo dictates that it would be incomplete for an objective image quality assessment of Veo reconstructions to consider only a single aspect of the two types of performance. The CHO analysis method used in this work

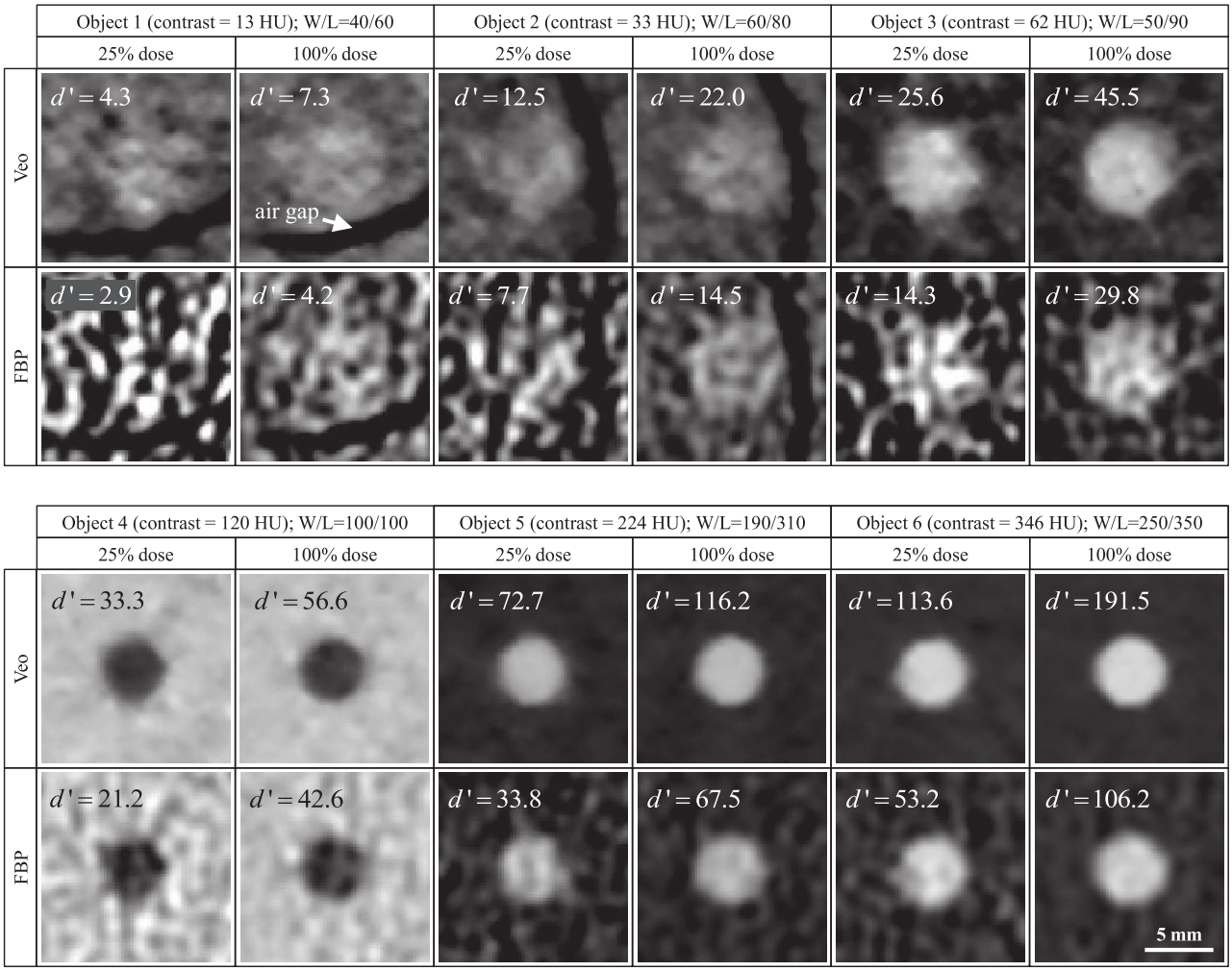

FIG. 11. CHO detectability indices (d') of the test objects. The ROI images were directly cropped from the original DICOM CT images. The scale bar applies to all.

took both into account. Figure 11 shows the CHO detectability indices d' of the detection tasks of six FOIs. The original noisy images are provided in the figure to help the readers directly evaluate their image quality. For both FBP and Veo, d' increased with object contrast and radiation dose; at any tested contrast/dose level, Veo always led to higher d' values, and therefore better overall CT image quality. The relative increase in d' varied between 33% and 114% depending on the contrast and dose level. These results have two indications: (1) For low contrast detection tasks, the influence of the aggressive noise reduction outweighs spatial resolution degradation in Veo; (2) For high contrast detection tasks, despite the relative increment in edge noise, the edge enhancement feature and the denoising feature in the surrounding uniform regions introduced by Veo can effectively improve the overall CT image quality.

4. DISCUSSION AND SUMMARY

By studying a commercially available implementation of MBIR, this work presented several key properties of the spatial resolution of this IR method: (1) The axial and z spatial resolution of MBIR improves with increasing radiation exposure level and increasing CT contrast level; (2) The spatial resolution of MBIR becomes equivalent to that of FBP at some intermediate contrast level, above which MBIR leads to superior spatial resolution (and vice versa). This "crossover" contrast highly depends on the radiation exposure level; (3) The PSFs of MBIR can be approximated as Gaussian functions with reasonably good accuracy, thus their experimental measurement can be potentially simplified by performing Gaussian fitting with noisy data. This is of practical value for quantifying the spatial resolution under low contrast and low dose conditions; (4) In MBIR, the trade-off between spatial resolution and noise is restricted to image pixels containing with steep contrast changes (i.e., at edges); (5) When both resolution and noise are considered, MBIR significantly improves the overall CT image quality. Some of these properties have been previously reported in an earlier work by Richard *et al.*,[15] who used a cylindrical and relatively uniform phantom to evaluate the axial spatial resolution of MBIR in the frequency domain. Reference 15 also showed the

dose-dependence of MBIR image noise measured in the uniform background region of the phantom. This work is expected to add further insight into the unique spatial resolution characteristics of MBIR. In addition, the experimental methodology developed in this work may add value to the practice of medical physics in the era of iterative CT reconstruction.

Due to the nonlinearity of the MBIR method, there is no closed-form formula to describe the experimental findings at the moment; there is also no theoretical method to analytically describe the contrast and dose dependence of spatial resolution either. However, it is feasible to qualitatively explain the physical origins of some of the findings using the basic principle and implementation method of MBIR reported in published literature: First, the contrast and dose dependence of the spatial resolution of MBIR can be primarily attributed to the use of an adaptive regularization method in MBIR; it automatically enforces stronger local smoothness (thus more blurring) for regions with low CNR and enforces stronger local sharpness for regions with high CNR. This explains why high contrast/low dose condition always leads to relatively superior spatial resolution and why low contrast/high dose condition always leads to relatively inferior spatial resolution. Second, the MBIR method, including the adaptive regularization, is implemented in three dimensional (3D) space, so it is not surprising that the z and axial spatial resolution demonstrated similar properties. Third, the spatial resolution of MBIR may also benefit from the improved modeling of system optics (e.g., finite focal spot size and detector pixel size), although a recent study showed that some implementations of ray modeling in IR may not play a signification role in improving spatial resolution with clinical CT conditions.[31]

The dose and contrast dependence of spatial resolution and its interplay with noise in MBIR suggests that there are significantly more challenges in optimizing CT protocols for this IR method. In conventional FBP-based linear CT systems, only a few scanning parameters (e.g., reconstruction kernel) influence spatial resolution, whereas in MBIR, spatial resolution is expected to be dependent on other settings (e.g., mA, gantry rotation time, helical pitch, contrast agent injective protocol) that directly or indirectly influence the dose and contrast level. The spatial resolution of MBIR also strongly depends on the imaging task and the patient: larger patients tend to lower detected x-ray signals and increase quantum noise, therefore may lead to degraded spatial resolution if other scanning parameters are fixed. As a result, the scanning protocols for MBIR must be further fine-tuned for each specific clinical application. It is likely that a much richer database provided by phantom studies and clinical validations would be necessary to rigorously optimize these protocols.

There are several limitations of this study that should be addressed: First, it only studied the axial scan mode and did not cover the helical scan mode. Unlike axial scan, helical scan may introduce misregistration between repeated scans due to patient couch translation. This problem of repeatability could potentially be addressed by performing image registration along the z direction. In future work, it would be interesting to study how the axial resolution and slice thickness of MBIR vary as a function of helical pitch and compare this with the relationship of FBP. Next, the restriction of our version of Veo to only allow a Head FOV with the axial scan mode prohibited the use of adult-sized phantoms. Once slice registration methods are developed, repeated helical scans in the Body scan FOV could potentially be performed to study the spatial resolution performance of MBIR as a function of patient size. Third, the current study only scanned the chest section of the phantom, and many of the features of interest were located near the center of the chest. As the statistical weighting factor in the data fidelity term of the MBIR objective function may also have a significant influence on the image quality, it would be interesting to study how spatial resolution of MBIR varies as a function of phantom shape, location of the feature, and local density distribution of the phantom. Fourth, the experimental study only covered a specific type of MBIR implemented by GE Healthcare; the image quality of MBIR is likely to vary across implementation methods. Even for a given CT vendor, the implementation of MBIR will continuously evolve and be improved upon, which may change the image properties such as the trade-off relationship between noise and resolution. Fifth, the noise standard deviation on the edges were calculated from repeated scans, which might also include inter-scan variation in CT number in the vicinity of FOI due to the nonlinear and statistical nature of the MBIR method. In addition, this measurement ignores noise spatial correlation. Due to these limitations, the specific numerical values determined to describe the spatial resolution properties of MBIR (e.g., the resolution crossover point between FBP and MBIR in Fig. 7) should not be generalized; instead, one should focus on the general characteristics of MBIR methods observed in this work.

In summary, the spatial resolution performance of the statistical MBIR method was experimentally characterized using a clinical CT system. Due to the intrinsic nonlinearity of the MBIR method, many well-known CT spatial resolution properties have been modified. In particular, dose dependence and contrast dependence have been introduced to the spatial resolution of CT images by MBIR. This method has also introduced some novel noise-resolution trade-offs not seen in traditional CT images. The benefits of MBIR are highlighted by the CHO study, which considered the joint contributions of spatial resolution and noise to the overall CT image quality.

ACKNOWLEDGMENTS

This work is partially supported by a NIH Grant No. R01CA169331 and GE Healthcare. The authors would like to thank Dr. Michael Speidel for providing the pediatric phantom.

[a]Author to whom correspondence should be addressed. Electronic mail: gchen7@wisc.edu.

[1]K. Sauer and C. Bouman, "A local update strategy for iterative reconstruction from projections," IEEE Trans. Signal Process. **41**, 534–548 (1993).

[2]J. Fessler and A. Hero, "Penalized maximum-likelihood image reconstruction using space-alternating generalized EM algorithms," IEEE Trans. Signal Process. **4**, 1417–1429 (1995).
[3]K. Lange and J. Fessler, "Globally convergent algorithms for maximum a posteriori transmission tomography," IEEE Trans. Signal Process. **4**, 1430–1438 (1995).
[4]C. Bouman and K. Sauer, "A unified approach to statistical tomography using coordinate descent optimization," IEEE Trans. Signal Process. **5**, 480–492 (1996).
[5]J.-B. Thibault, K. D. Sauer, C. A. Bouman, and J. Hsieh, "A three-dimensional statistical approach to improved image quality for multislice helical CT," Med. Phys. **34**, 4526–4544 (2007).
[6]G.-H. Chen, J. Tang, and S. Leng, "Prior image constrained compressed sensing (PICCS): A method to accurately reconstruct dynamic CT images from highly undersampled projection data sets," Med. Phys. **35**, 660–663 (2008).
[7]P. Thèriault-Lauzier and G.-H. Chen, "Characterization of statistical prior image constrained compressed sensing. I. Applications to time-resolved contrast-enhanced CT," Med. Phys. **39**, 5930–5948 (2012).
[8]P. Thériault-Lauzier and G.-H. Chen, "Characterization of statistical prior image constrained compressed sensing (PICCS): II. Application to dose reduction," Med. Phys. **40**, 021902 (14pp.) (2013).
[9]Z. Yu, J.-B. Thibault, C. Bouman, K. Sauer, and J. Hsieh, "Fast model-based x-ray CT reconstruction using spatially nonhomogeneous ICD optimization," IEEE Trans. Image Proces. **20**, 161–175 (2011).
[10]P. J. Pickhardt, M. G. Lubner, D. H. Kim, J. Tang, J. A. Ruma, A. M. del Rio, and G.-H. Chen, "Abdominal CT with model-based iterative reconstruction (MBIR): Initial results of a prospective trial comparing ultralow-dose with standard-dose imaging," Am. J. Roentgenol. **199**, 1266–1274 (2012).
[11]K. Yasaka, M. Katsura, M. Akahane, J. Sato, I. Matsuda, and K. Ohtomo, "Model-based iterative reconstruction for reduction of radiation dose in abdominopelvic CT: Comparison to adaptive statistical iterative reconstruction," SpringerPlus **2**, 209 (9pp.) (2013).
[12]E. A. Smith, J. R. Dillman, M. M. Goodsitt, E. G. Christodoulou, N. Keshavarzi, and P. J. Strouse, "Model-based iterative reconstruction: Effect on patient radiation dose and image quality in pediatric body CT," Radiology **0**, 130362 (2013).
[13]B. Chen, H. Barnhart, S. Richard, M. Robins, J. Colsher, and E. Samei, "Volumetric quantification of lung nodules in CT with iterative reconstruction (ASiR and MBIR)," Med. Phys. **40**, 111902 (10pp.) (2013).
[14]D. Pal, S. Kulkarni, G. Yadava, J.-B. Thibault, K. Sauer, and J. Hsieh, "Analysis of noise power spectrum for linear and non-linear reconstruction algorithms for CT," in *IEEE Nuclear Science Symposium and Medical Imaging Conference (NSS/MIC)* (IEEE, Valencia, Spain, 2011), pp. 4382–4385.
[15]S. Richard, D. B. Husarik, G. Yadava, S. N. Murphy, and E. Samei, "Towards task-based assessment of CT performance: System and object MTF across different reconstruction algorithms," Med. Phys. **39**, 4115–4122 (2012).
[16]B. Chen, S. Richard, and E. Samei, "Relevance of MTF and NPS in quantitative CT: Towards developing a predictable model of quantitative performanace," Proc. SPIE **8313**, 83132O (2012).
[17]K. Li, T. Jie, and G.-H. Chen, "Statistical model based iterative reconstruction (MBIR) in clinical CT systems: Experimental assessment of noise performance," Med. Phys. **41**, 041906 (15pp.) (2014).
[18]P. Thériault-Lauzier, J. Tang, and G.-H. Chen, "Prior image constrained compressed sensing: Implementation and performance evaluation," Med. Phys. **39**, 66–80 (2012).
[19]J. Solomon and E. Samei, "Are uniform phantoms sufficient to characterize the performance of iterative reconstruction in CT?" Proc. SPIE **8668**, 86684M (2013).
[20]J. R. Bushberg, J. A. Seibert, J. Edwin M. Leidholdt, and J. M. Boone, *The Essential Physics of Medical Imaging* (Lippincott Wilkiams & Wilkins, Philadelphia, 2001).
[21]I. S. Kyprianou, S. Rudin, D. R. Bednarek, and K. R. Hoffmann, "Generalizing the MTF and DQE to include x-ray scatter and focal spot unsharpness: Application to a new microangiographic system," Med. Phys. **32**, 613–626 (2005).
[22]P. Prakash, W. Zbijewski, G. J. Gang, Y. Ding, J. W. Stayman, J. Yorkston, J. A. Carrino, and J. H. Siewerdsen, "Task-based modeling and optimization of a cone-beam CT scanner for musculoskeletal imaging," Med. Phys. **38**, 5612–5629 (2011).
[23]E. Nickoloff and R. Riley, "A simplified approach for modulation transfer function determinations in computed tomography," Med. Phys. **12**, 437–442 (1985).
[24]K. Li, J. Zambelli, N. Bevins, Y. Ge, and G.-H. Chen, "Spatial resolution characterization of differential phase contrast CT systems via modulation transfer function (MTF) measurements," Phys. Med. Biol. **58**, 4119–4135 (2013).
[25]K. J. Myers and H. H. Barrett, "Addition of a channel mechanism to the ideal-observer model," J. Opt. Soc. Am. A **4**, 2447–2457 (1987).
[26]C. K. Abbey, H. H. Barrett, and D. W. Wilson, "Observer signal-to-noise ratios for the ML-EM algorithm," Proc. SPIE **2712**, 47–58 (1996).
[27]A. E. Burgess, X. Li, and C. K. Abbey, "Visual signal detectability with two noise components: Anomalous masking effects," J. Opt. Soc. Am. A **14**, 2420–2442 (1997).
[28]H. C. Gifford, M. A. King, D. J. de Vries, and E. J. Soares, "Channelized Hotelling and human observer correlation for lesion detection in hepatic SPECT imaging," J. Nucl. Med. **41**, 514–521 (2000).
[29]A. E. Burgess, F. L. Jacobson, and P. F. Judy, "Human observer detection experiments with mammograms and power-law noise," Med. Phys. **28**, 419–437 (2001).
[30]L. Yu, S. Leng, L. Chen, J. M. Kofler, R. E. Carter, and C. H. McCollough, "Prediction of human observer performance in a 2-alternative forced choice low-contrast detection task using channelized Hotelling observer: Impact of radiation dose and reconstruction algorithms," Med. Phys. **40**, 041908 (9pp.) (2013).
[31]C. Hofmann, M. Knaup, and M. Kachelriess, "Effects of ray profile modeling on resolution recovery in clinical CT," Med. Phys. **41**, 021907 (14pp.) (2014).